Aluminum Nanosized Beams as Probes of Superfluid ^{4}He

M. T. Noble,[1] A. Guthrie,[1, a)] A. Jennings,[1, b)] S. Kafanov,[1] M. Poole,[1] M. Sarsby,[1, a)] T. Wilcox,[1] and V. Tsepelin[1]

Department of Physics, Lancaster University, Lancaster, LA1 4YB, United Kingdom

(*Electronic mail: v.tsepelin@lancaster.ac.uk)

(Dated: 25 July 2024)

Sub-micrometer-size devices are strong candidates for future use as probes of quantum fluids. They can be reproducibly manufactured with resonant frequencies in the range of kilohertz to gigahertz and have low power consumption and dissipation. Here, we present doubly clamped aluminum nanobeams of lengths from 15 µm up to 100 µm operated in vacuum and the hydrodynamic regime of liquid ^{4}He. We observe that in vacuum devices are described well using a simple harmonic motion with a constant Duffing coefficient and in helium quantitatively model their behavior with the conventional hydrodynamic model.

PACS numbers: Valid PACS appear here
Keywords: Suggested keywords

Superfluid research has benefited from improvements in nanofabrication facilities and their availability, which have promoted a wider utilization of micro- and nanoelectromechanical systems (MEMS and NEMS). The high force sensitivity, small mass, and size of MEMS and NEMS make them ideal local probes in superfluid ^{4}He[1–6] and ^{3}He[7–9]. In superfluid ^{4}He, NEMS can produce and detect excitations such as rotons and phonons[10–13]. Furthermore, they have opened up new avenues for studying topological defects in quantum fluids: a MEMS resonator detected the presence of remnant quantum vortices on device dynamics[6], and a nanobeam NEMS captured and trapped single quantum vortices along its length[14]. In superfluid ^{3}He-B, the NEMS dimensions approach the superfluid coherence length but their adaptation has been slower owing to the more stringent environment requirements. So far, MEMS and NEMS devices have been utilized to study Andreev bound states[7], Bogoliubov quasiparticles[8,9] and to visualize a tangle of quantum vortices using a 5 by 5 pixel quasiparticle camera[15]. Practical applications of submerging devices in superfluid ^{4}He include determining the intrinsic damping mechanism of NEMS due to two-level systems[13], and improving the sensitivity of the optomechanical setup as a result of better cooling[16]. Systematic studies of quantum turbulence or search for dark matter using superfluid ^{3}He[9] rely on the availability of arrays of NEMS and here we assess how similar results are obtained using aluminum beams of varying lengths, manufactured on a silicon substrate by a nominally identical process. Technologically such beams are easy to fabricate, and at low temperatures they are tensioned due to thermal contraction mismatch and have mechanical properties similar to prestressed Si_3N_4 structures. Furthermore, aluminum on bare silicon offers the possibility to integrate low-frequency NEMS into microwave resonators and create optomechanical devices with enhanced sensitivities[17].

We present the results of five doubly-clamped aluminum beams patterned using electron-beam lithography on a silicon substrate, followed by aluminum deposition, and reactive ion etching. Beams have lengths, ℓ, of 15 µm, 25 µm, 50 µm, 75 µm and 100 µm with a rectangular cross section of height $h \simeq 100$ nm and width $w \simeq 160$ nm. The beams are suspended 2 microns above the substrate. Figure 1 shows a scanning electron microscope image of the 25 µm beam and the magnetomotive measurement scheme that is employed to excite and detect beams' motion. A vector network analyzer (VNA) drives the beams in a magnetic field, B, of 5 T. The voltage output of the VNA, $V_{\rm out}$, is decreased using an attenuator, A, by a factor of 60 dB or 80 dB. The circuit impedance, Z, converts the attenuated voltage into a current, and the resulting Laplace force causes the beam to vibrate in the plane of the chip. The beam's motion in a magnetic field gives rise to a Faraday electromotive force (EMF) voltage that is amplified at room temperature with a power gain, G, 40 dB or 80 dB and subsequently recorded by the VNA as the transmission signal S_{21}. The inset of the Fig. 1 shows a frequency response of a 25 µm beam in vacuum at 4.2 K in the vicinity of resonance at low excitation power.

Our detection setup is a 2-terminal measurement. The total impedance of the circuit Z is expected to be dominated by the resistance of the beams due to their small dimensions and is calculated using the expression:

$$Z = 2\left(\frac{AG}{S_{21}} - 1\right) Z_{50}, \tag{1}$$

where S_{21} is off-resonance signal and $Z_{50} = 50\,\Omega$ is the impedance of the amplifier. We observe that Z scales as the length of the beam except for the 100 µm-long beam, which exhibits several times higher resistance. The extracted value of the resistivity of aluminum for our beams, $6.8 \times 10^{-8}\,\Omega$m, is the same in a vacuum and liquid helium and is consistent with the results reported for 100 nm-thick aluminum films[18]. Identical resistance in vacuum and helium shows that at a temperature of 4.2 K the beams are thermalized even without being submerged in liquid.

The motion of a large oscillating wire can be described by

a)Now at: IQM Quantum Computers, Keilaranta 19, Espoo, 02150, Finland.
b)Now at: RIKEN Centre for Quantum Computing, RIKEN, Wako, 351-0198, Japan.

a simple harmonic motion[19], however, nanosized beams exhibit nonlinear behavior at large drives[1,20,21], and we model observed behavior by adding a Duffing term[22], αx^3, to the linear equation of an externally driven harmonic oscillator:

$$\ddot{x} + \lambda\dot{x} + (2\pi f_0)^2 x + \alpha x^3 = \mathscr{F} e^{2\pi i f t}. \tag{2}$$

Here x is the beam's displacement, λ is the linear damping coefficient, α is the Duffing parameter, and f is the driving frequency. The natural frequency of the resonator $f_0 = (2\pi)^{-1}\sqrt{k/m}$ is determined by the effective spring constant k and the effective mass of a beam m. The amplitude of the drive force normalized to a beam mass is $\mathscr{F}$.

We obtain the driving force from:

$$F = \sqrt{\xi}\frac{S_{21}V_{\text{out}}}{GZ_{50}}B\ell, \tag{3}$$

where the numerical factor ξ is determined by the beam mode (0.3965 for the fundamental mode of the doubly clamped beam[23]). A magnitude of the resonance dip ΔS_{21} yields the Faraday EMF and is used for inferring the beam velocity:

$$\dot{x} = \frac{2}{\sqrt{\xi}}\frac{\Delta S_{21}}{S_{21}}\frac{AV_{\text{out}}}{B\ell}. \tag{4}$$

The main panel in the Fig. 2 shows a color map of frequency sweeps as a function of force for 25 µm beam in vacuum. At low drives, the resonance frequency of the beam is 4.60 MHz and seems to be increasing as a function of drive force towards 4.68 MHz. At low drives the contribution of the Duffing term is negligible, and the least-square fitting of the Lorentzian line shape allows us to determine the resonant frequency f_0, the damping width $\Delta f = \lambda/2\pi$, the depth of the dip ΔS_{21} and the

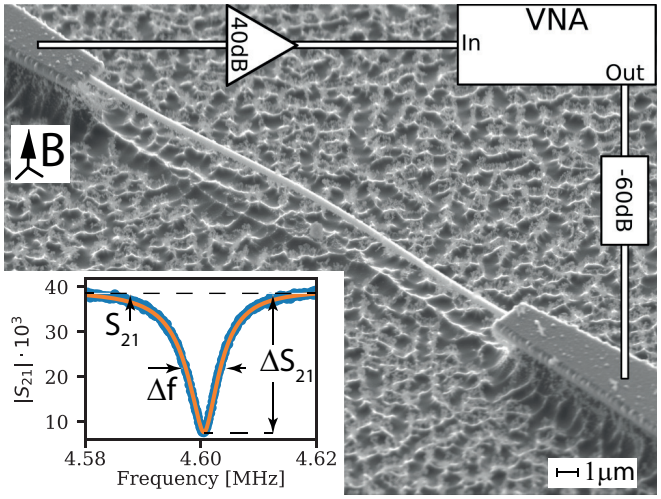

FIG. 1. A scanning electron microscope image of the 25 µm beam with a diagram of the measurement setup. The buckling of the beam disappears at low temperatures due to the difference in the thermal contraction of the aluminum and the silicon substrate. Inset: Frequency response of the 25 µm beam in vacuum at 4.2 K. The experimental data points are plotted with light blue color while the Lorentzian fit is illustrated using orange.

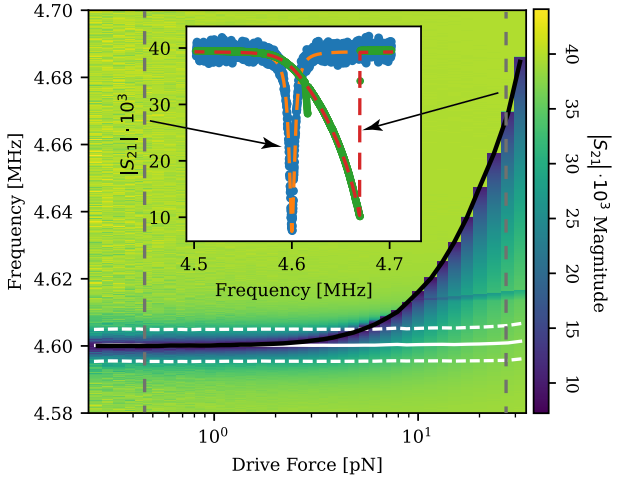

FIG. 2. Colour map of frequency sweeps with increasing force for the 25 µm beam. The solid black line tracks the maximum response while the white solid and dashed lines show the inferred resonance frequency and width, respectively. Inset: two frequency sweeps at low power (blue) and high power (green). We fit the measured values with Lorentzian or Duffing equations (orange and red dashed lines correspondingly).

background S_{21} (see inset of Fig. 1 for an example). At high excitations, the beam response is no longer Lorentzian, and we follow the methods described in the references[22,24] to fit a Duffing resonance curve. Fitting the measured resonances using the Duffing equation (Eq. (2)) reveals that the natural resonance frequency and resonance width observed at low drive remain constant (white solid and dashed lines), and the apparent shift of the resonance (solid black line) is governed by a constant Duffing term. The inset demonstrates fits of the frequency sweeps using Lorentzian and Duffing line shapes at low and high drives, respectively.

The difference in the thermal contraction of the aluminum beam and the silicon substrate gives rise to the tension of the beam at low temperatures. We have determined the tensile strain $\mathscr{T}$ from the measured resonance frequency using the following equation[19]:

$$f_{0,\,\text{vac}} = \frac{4.730^2}{\pi\sqrt{48}}\frac{w}{\ell^2}\sqrt{\frac{E}{\rho_b}}\sqrt{1 + 0.2949\left(\frac{\ell}{w}\right)^2\frac{\mathscr{T}}{whE}}, \tag{5}$$

where $E = 70\,\text{GPa}$ is the Young's modulus, and $\rho_b = 2700\,\text{kg m}^{-3}$ is the aluminum beam density. The shortest beams have highest tension, which may indicate the importance of clamping effects.

Table I summarizes parameters that we have extracted from the vacuum frequency sweeps for the measured beams. The moderate values of the vacuum Q-factor, $f_{0,\,\text{vac}}/\Delta f$, ranging from 10^2 to 10^3, can be attributed to the high magnetic field of 5 T. The magnetic field's quadratic effect on damping is well known for the magnetomotive driving scheme[25].

The ratio of inferred m and theoretical m_{th} effective masses:

$$\chi_m \equiv \frac{m}{m_{\text{th}}} = \frac{F}{2\pi\Delta f\dot{x}}\frac{1}{\xi\rho_b wh\ell}, \tag{6}$$

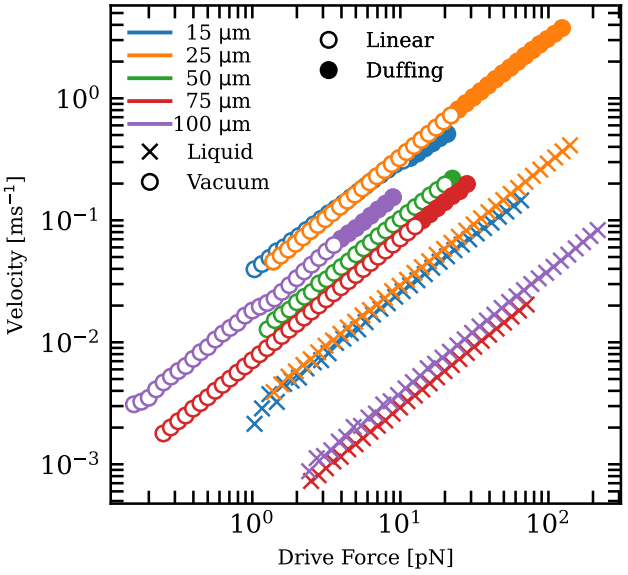

FIG. 3. Velocity versus force for the 15 µm (blue), 25 µm (orange), 50 µm (green), 75 µm (red) and 100 µm (purple) beams in vacuum (circles) and superfluid helium below 1.6 K (crosses). The filled circles show where the inclusion of the Duffing term is required for accurate fitting of the frequency sweeps in a vacuum.

is within an order of magnitude of unity and together with the accepted value of resistivity indicates that our 2-terminal measurement scheme yields correct results.

The most striking observation is an arbitrary sign of the Duffing term α for our beams despite an identical manufacturing process. Systematic measurements utilizing scanning force microscopy of the beam surface and substrate are required to understand what governs the sign of Duffing nonlinearity. The shortest, 15 µm-long, beam has the largest values of the spring constant and Duffing term but their ratio is similar to other beams and observed non-linearity behaves likewise. Fully suspended Si_3N_4 beams with an aluminum conducting layer have been reported to have a similar value of the spring constant and an order of magnitude lower Duffing parameter[21].

Figure 3 summarizes the velocity-force relationship for the beams in vacuum (circles) and superfluid helium (crosses) at temperatures below 1.6 K, respectively. Each point in the figure is the result of the fitting of a frequency sweep and the application of Eqs. 3 and 4. In a vacuum, the frequency sweeps corresponding to Lorentzian and Duffing line shapes

TABLE I. Parameters of aluminium nanobeams in vacuum.

ℓ [µm]	$f_{0,\,\mathrm{vac}}$ [MHz]	$\mathscr{T}$ [µN]	Δf [kHz]	Z [kΩ]	χ_m	k [N m^{-1}]	α [m^{-2} s^{-2}]
100	0.6028	0.5	1.5	2.1	3.5	0.086	-1.3×10^{26}
75	0.9716	0.7	3.2	0.37	5.4	0.26	-4.7×10^{26}
50	1.187	0.5	11.1	0.21	1.6	0.076	6.8×10^{26}
25	4.60	1.7	9.6	0.15	1.2	0.42	26×10^{26}
15	8.469	1.8	7.5	0.10	2.6	1.9	-7×10^{28}

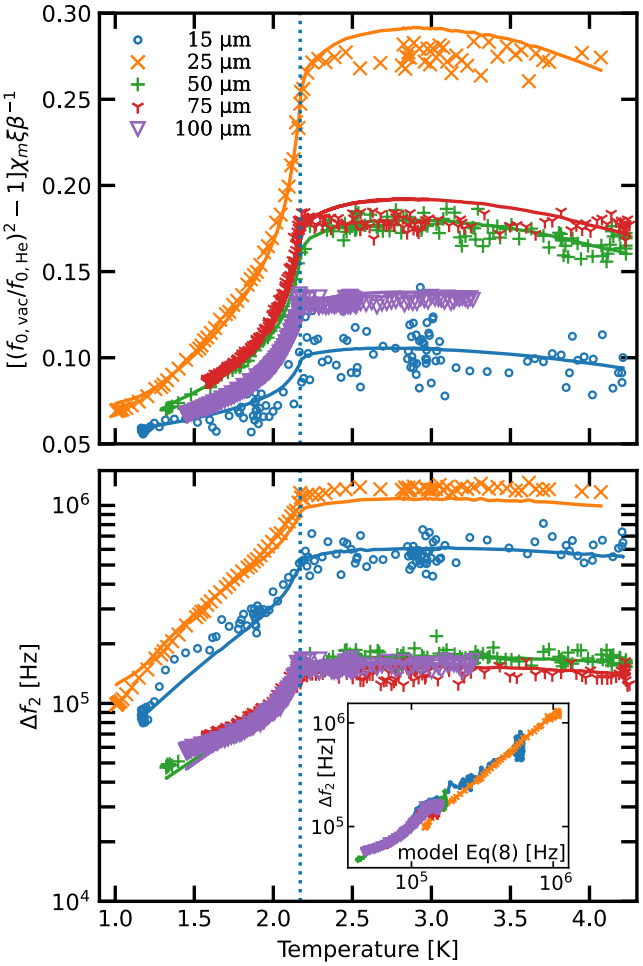

FIG. 4. The temperature dependence of the beams in liquid helium, the lines show fits using the model (see text). The vertical blue dotted line indicated a phase transition temperature from normal to superfluid phase. (Top) The square of the ratio of vacuum frequency over the resonance in helium against the temperature. (Bottom) The temperature dependence of the width. (Inset) The measured widths of the nanobeams vs the normalised frequency ratio $(f_{0,\,\mathrm{He}}/f_{0,\,\mathrm{vac}})^2$ calculated with Eq. (8) (see text).

are denoted by empty and filled circles correspondingly. The observed superfluid damping is significantly higher than in a vacuum since we work at temperatures above 1 K, in the so-called hydrodynamic regime, and all helium data are well described by Lorentzian line shapes. However, when similar studies are carried out in pure superfluid, at temperatures below 0.5 K, such as in[11,13], knowledge of the Duffing coefficients of intrinsic beam behavior is essential.

In liquid helium above 1 K, the main source of damping comes from the fluid viscosity η that drags on the beam as it vibrates. Even with 10% of normal fluid at a temperature of 1.5 K damping in helium exceeds the vacuum damping in a magnetic field of 5 T by an order of magnitude. We characterize this damping by following a hydrodynamic model[26,27] and similarly assume that the spring constant is unchanged by submerging beams in helium and consequently $(f_{0,\,\mathrm{vac}}/f_{0,\,\mathrm{He}})^2 =$

m_{He}/m. The mass of the beam m_{He} in liquid is enhanced by the contributions of fluid displaced by the beam, so-called backflow, and normal fluid trapped around the beam due to the viscous penetration depth $\delta_n = \sqrt{\eta/(\pi\rho_n f_{0,\,\mathrm{He}})}$. The ratio of vacuum $f_{0,\,\mathrm{vac}}$ and liquid $f_{0,\,\mathrm{He}}$ frequencies can be expressed as:

$$\left(\frac{f_{0,\,\mathrm{vac}}}{f_{0,\,\mathrm{He}}}\right)^2 - 1 = \frac{1}{\chi_m \xi}\frac{\rho_{\mathrm{He}}}{\rho_b}\left(\beta + B\frac{S\delta_n}{V}\frac{\rho_{\mathrm{n}}}{\rho_{\mathrm{He}}}\right), \qquad (7)$$

where the first term on the RHS is the backflow proportional to the volume of the oscillating body and the second term characterizes viscous fluid clamped around the oscillator. Here ρ_{He} is the total density of liquid helium, ρ_n is the density of the normal fluid component, β and B are the fitting parameters with theoretical values of $\beta = \pi h/(4w) = 0.785$ and $B = 1$[28]. The ratio of surface S to volume V for our beams is equal to $2(w+h)/(wh) = 3.25\times10^{-11}\,\mathrm{m}^{-1}$.

The top of Fig. 4 shows the normalized LHS of Eq. (7) as a function of temperature. The observed temperature dependence is dominated by the second term of Eq. (7) due to the presence of viscosity and the normal component density of helium. In the absence of a normal fluid component, the RHS of Eq. (7) for all beams should asymptotically reach $5.4\times10^{-2}\beta/(\chi_m\xi)$. The solid lines correspond to the fitting of the model and yield parameters β and B that are listed in the Table II. The bottom of Fig. 4 shows the dependence of the resonant width for the beams as a function of temperature. The solid lines are fits using the following model[26]:

$$\Delta f = \frac{1}{2\pi}\frac{CB}{\chi_m\xi\rho_b}\frac{S}{V}\frac{\eta}{\delta_n}\left(\frac{f_{0,\,\mathrm{He}}}{f_{0,\,\mathrm{vac}}}\right)^2 + \Delta f_{\mathrm{vrt}}, \qquad (8)$$

where C is a fitting parameter characterizing the flow around the beam and is expected to be equal to 2[29]. The non-thermal width, Δf_{vrt}, is determined via fitting and varies considerably between the beams and changes after passing through the normal to superfluid transition. In earlier works[1,11] we attributed the excess of non-thermal damping in the liquid to the acoustic emission of the beam. Recently we observed that the damping of a beam in vacuum and pure superfluid is almost identical when the experimental cell is filled with helium at temperatures well below the superfluid transition[14]. Hence, the excess damping cannot come from the acoustical emission as the beam sizes and frequencies are same order of magnitude. We conclude that non-thermal damping is governed by a large number of trapped vortices during the transition. This picture is consistent with the work of Barquist *et al.*[6] that has observed annealing of damping on MEMS devices.

The inset in Fig. 4 compares the behavior of beams by presenting the measured resonance width as a function of the frequency ratio $(f_{0,\,\mathrm{vac}}/f_{0,\,\mathrm{He}})^2$ with the corresponding numerical parameters. Specifically, we use the entire right-hand side of Eq. (8) to collapse temperature dependence data.

To contrast the measured force-velocity and temperature dependencies for the beams, we investigate the behavior of a drag coefficient C_{D} as a function of the Donnelly number D_n. The Donnelly number is an analogue of the boundary-layer-based Reynolds number in the superfluid phase of helium and becomes identical to it in the normal phase[27]. The dimensionless drag coefficient is defined as follows:

$$C_{\mathrm{D}} = \frac{2F}{A\rho_n\dot{x}^2}, \qquad (9)$$

where A is the sectional area perpendicular to the direction of flow. The Donnelly number is given by:

$$D_n = \frac{\delta_n\rho_n\dot{x}}{\eta}. \qquad (10)$$

Analysis of the power dissipation due to the hydrodynamic drag shows that the relationship between both quantities is governed purely by geometric coefficients[27]:

$$C_{\mathrm{D}} = CB\frac{2S}{A}\frac{1}{D_n}. \qquad (11)$$

Figure 5 plots the drag coefficient C_{D} as a function of the Donnelly number D_n normalized by CB in helium for amplitude and temperature measurements, which were presented in Fig. 3 and Fig. 4. The amplitude and temperature sweeps agree with each other. The slope in the log-log plot equal to -1 shows that all beams are in the laminar regime. For our beams, the ratio of the surfaces S/A is expected to be identical and Fig. 5 shows that data collapses for three of the beams. The dependencies of the 25 μm and 75 μm beams require corrections 1.5 and 0.6 times, respectively, indicating that the helium flow experienced by the total surface and the sectional

TABLE II. Parameters of the beams in liquid helium.

ℓ [μm]	β	B	C	Δf_{vrt} [kHz]
100	6.3	2.4	2.6	10
75	3.5	3.0	1.6	34
50	0.72	0.63	2.5	15
25	0.62	1.9	2.4	0
15	0.57	0.57	5.8	21

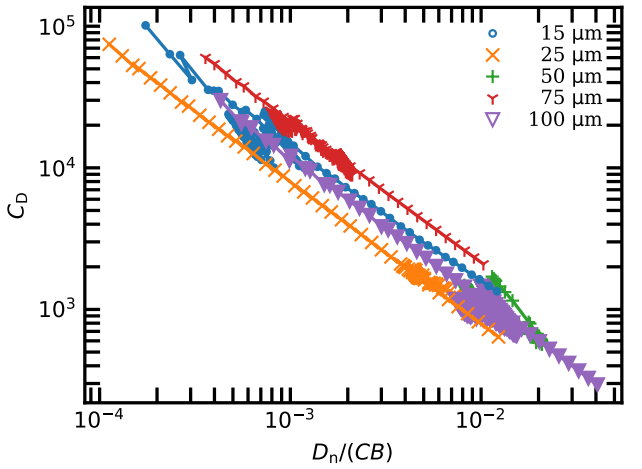

FIG. 5. The dependence of drag coefficient C_{D} on the Donnelly number D_n divided by the product of C and B for the amplitude and temperature sweeps in helium.

area perpendicular to the direction of the flow scales differently.

Overall, we conclude that all of our nanomechanical beams behave similarly both in vacuum and in liquid helium. In a vacuum, the Duffing non-linearity dominates their behavior at displacement amplitudes in excess of $\sim$10 nm and will need to be accounted for in the pure superfluid. In helium, modeling the beams with a Stokes' drag model is possible despite the viscous penetration depth being comparable to the width and height of the beams themselves. Due to the small size and proximity of the substrate surface, the beams require verification of parameters and cannot be operated under the assumption that their effective mass and expected geometric coefficients match the theory within 10%, as is the case with larger objects such as quartz tuning forks[30].

ACKNOWLEDGMENTS

The research leading to these results was supported by UKRI EPSRC and STFC (Grants ST/T006773/1, EP/P022197/1 and EP/X004597/1), as well the European Union's Horizon 2020 Research and Innovation Programme under Grant Agreement no 824109 (European Microkelvin Platform).

AUTHOR DECLARATIONS

Conflict of Interest

The authors have no conflicts to disclose.

Author Contributions

M. T. Noble: Conceptualization (equal); Data Curation (equal); Formal Analysis (equal); Investigation (equal); Writing - Review & Editing (equal). **A. Guthrie:** Conceptualization (equal); Data Curation (equal); Formal Analysis (equal); Investigation (equal); Methodology (equal). **A. Jennings:** Conceptualization (equal); Data Curation (supporting); Formal Analysis (equal); Investigation (equal); Writing - Original Draft (equal); **S. Kafanov:** Conceptualization (lead); Data Curation (equal); Formal Analysis (equal); Funding Acquisition (equal); Methodology (lead); Project Administration (equal); Supervision (lead); Writing - Original Draft (equal); Writing - Review & Editing (equal). **M. Poole:** Conceptualization (equal); Data Curation (equal); Methodology (equal). **M. Sarsby:** Conceptualization (equal); Data Curation (equal); Formal Analysis (equal); Methodology (equal). **T. Wilcox:** Conceptualization (equal); Formal Analysis (equal); Writing - Original Draft (equal). **V. Tsepelin:** Conceptualization (equal); Formal Analysis (lead); Funding Acquisition (equal); Investigation (equal); Project Administration (equal); Supervision (equal); Writing - Original Draft (equal); Writing - Review & Editing (lead).

DATA AVAILABILITY

The data that support the findings of this study are openly available at the Lancaster University Data Repository at https://doi.org/, reference number [XX].

[1] D. I. Bradley, R. George, A. M. Guénault, R. P. Haley, S. Kafanov, M. T. Noble, Yu. A. Pashkin, G. R. Pickett, M. Poole, J. R. Prance, M. Sarsby, R. Schanen, V. Tsepelin, T. Wilcox, and D. E. Zmeev, Scientific Reports **7**, 4876 (2017).
[2] T. Kamppinen and V. B. Eltsov, J. Low Temp. Phys. **196**, 283 (2019).
[3] Š. Midlik, J. Sadílek, Z. Xie, Y. Huang, and D. Schmoranzer, J. Low Temp. Phys. **208**, 475 (2022).
[4] G. I. Harris, D. L. McAuslan, E. Sheridan, Y. Sachkou, C. Baker, and W. P. Bowen, Nat. Phys. **12**, 788 (2016).
[5] M. Gonzalez, P. Bhupathi, B. H. Moon, P. Zheng, G. Ling, E. Garcell, H. B. Chan, and Y. Lee, Journal of Low Temperature Physics **162**, 661 (2011).
[6] C. S. Barquist, W. G. Jiang, K. Gunther, N. Eng, Y. Lee, and H. B. Chan, Phys. Rev. B **101**, 174513 (2020).
[7] P. Zheng, W. G. Jiang, C. S. Barquist, Y. Lee, and H. B. Chan, Phys. Rev. Lett. **117**, 195301 (2016).
[8] M. Defoort, S. Dufresnes, S. L. Ahlstrom, D. I. Bradley, R. P. Haley, A. M. Guénault, E. A. Guise, G. R. Pickett, M. Poole, A. J. Woods, V. Tsepelin, S. N. Fisher, H. Godfrin, and E. Collin, J. Low Temp. Phys. **183**, 284 (2016).
[9] S. Autti, A. Casey, N. Eng, N. Darvishi, P. Franchini, R. P. Haley, P. J. Heikkinen, A. Jennings, A. Kemp, E. Leason, L. V. Levitin, J. Monroe, J. March-Russel, M. T. Noble, J. R. Prance, X. Rojas, T. Salmon, J. Saunders, R. Smith, M. D. Thompson, V. Tsepelin, S. M. West, L. Whitehead, V. V. Zavjalov, D. E. Zmeev, and Q.-D. collaboration, The European Physical Journal C **84**, 248 (2024).
[10] K. Y. Fong, D. Jin, M. Poot, and H. X. Tang, Nano Lett. **19**, 3716 (2019).
[11] A. M. Guénault, A. Guthrie, R. P. Haley, S. Kafanov, Yu. A. Pashkin, G. R. Pickett, M. Poole, R. Schanen, V. Tsepelin, D. E. Zmeev, E. Collin, O. Maillet, and R. Gazizulin, Phys. Rev. B **100**, 020506(R) (2019).
[12] A. M. Guénault, A. Guthrie, R. P. Haley, S. Kafanov, Yu. A. Pashkin, G. R. Pickett, V. Tsepelin, D. E. Zmeev, E. Collin, R. Gazizulin, and O. Maillet, Phys. Rev. B **101**, 060503(R) (2020).
[13] T. Kamppinen, J. T. Mäkinen, and V. B. Eltsov, Physical Review B **107**, 014502 (2023).
[14] A. Guthrie, S. Kafanov, M. T. Noble, Yu. A. Pashkin, G. R. Pickett, V. Tsepelin, A. A. Dorofeev, V. A. Krupenin, and D. E. Presnov, Nat. Commun. **12**, 1 (2021).
[15] M. T. Noble, S. L. Ahlstrom, D. I. Bradley, E. A. Guise, R. P. Haley, S. Kafanov, G. R. Pickett, M. Poole, R. Schanen, T. Wilcox, A. J. Woods, D. E. Zmeev, and V. Tsepelin, Phys. Rev. B **105**, 174515 (2022).
[16] L. A. De Lorenzo and K. C. Schwab, New J. Phys. **16**, 113020 (2014).
[17] M. Sillanpää, J. Sarkar, J. Sulkko, J. Muhonen, and P. J. Hakonen, Appl. Phys. Lett. **95**, 011909 (2009).
[18] A. F. Mayadas, Journal of Applied Physics **38**, 4241–4245 (1968).
[19] M. Bao, *Analysis and Design Principles of MEMS Devices* (Elsevier, 2005).
[20] S. Kumar, S. Rebari, S. P. Pal, S. S. Yadav, A. Kumar, A. Aggarwal, S. Indrajeet, and A. Venkatesan, Nano Letters **21**, 2975 (2021), https://doi.org/10.1021/acs.nanolett.1c00109.
[21] I. Golokolenov, B. Alperin, B. Fernandez, A. Fefferman, and E. Collin, Journal of Low Temperature Physics **210**, 550 (2023).
[22] R. Lifshitz and M. C. Cross, "Nonlinear Dynamics of Nanomechanical and Micromechanical Resonators," in *Reviews of Nonlinear Dynamics and Complexity* (John Wiley & Sons, Ltd, 2008) Chap. 1, pp. 1–52.
[23] B. D. Hauer, C. Doolin, K. S. D. Beach, and J. P. Davis, Annals of Physics **339**, 181 (2013).
[24] E. Collin, Yu. M. Bunkov, and H. Godfrin, Phys. Rev. B **82**, 235416 (2010).
[25] A. P. J. Voncken, J. H. Naish, J. R. Owers-Bradley, R. König, D. Riese, and F. Pobell, J. Low Temp. Phys. **110**, 1105 (1998).
[26] R. Blaauwgeers, M. Blazkova, M. Človečko, V. B. Eltsov, R. de Graaf, J. Hosio, M. Krusius, D. Schmoranzer, W. Schoepe, L. Skrbek, P. Skyba, R. E. Solntsev, and D. E. Zmeev, J. Low Temp. Phys. **146**, 537 (2007).

[27] D. Schmoranzer, M. J. Jackson, Š. Midlik, M. Skyba, J. Bahyl, T. Skokánková, V. Tsepelin, and L. Skrbek, Physical Review B **99**, 054511 (2019).
[28] J. E. Sader, J. Appl. Phys. **84**, 64 (1998).
[29] L. D. Landau and E. M. Lifshitz, *Fluid Mechanics, Second Edition: Vol. 6 (Course of Theoretical Physics)*, 2nd ed. (Butterworth-Heinemann, 1987).
[30] V. Tsepelin, S. Ahlstrom, I. Bradley, M. Clovecko, S. Fisher, T. Guénault, E. A. Guise, R. Haley, O. Kolosov, P. V. E. McClintock, G. Pickett, M. Poole, and A. Woods, Physical review B **89** (2014), 10.1103/PhysRevB.89.014515.